Slower nutrient stream suppresses Subarctic Atlantic Ocean biological productivity in global warming

Daniel B. Whitt[a,1] and Malte F. Jansen[b]

[a]Climate and Global Dynamics Laboratory, National Center for Atmospheric Research, Boulder, CO 80307; and [b]Department of the Geophysical Sciences, The University of Chicago, Chicago, IL 60637

Edited by Edward A. Boyle, Massachusetts Institute of Technology, Cambridge, MA, and approved May 18, 2020 (received for review January 15, 2020)

Earth system models (ESMs) project that global warming suppresses biological productivity in the Subarctic Atlantic Ocean as increasing ocean surface buoyancy suppresses two physical drivers of nutrient supply: vertical mixing and meridional circulation. However, the quantitative sensitivity of productivity to surface buoyancy is uncertain and the relative importance of the physical drivers is unknown. Here, we present a simple predictive theory of how mixing, circulation, and productivity respond to increasing surface buoyancy in 21st-century global warming scenarios. With parameters constrained by observations, the theory suggests that the reduced northward nutrient transport, owing to a slower ocean circulation, explains the majority of the reduced productivity in a warmer climate. The theory also informs present-day biases in a set of ESM simulations as well as the physical underpinnings of their 21st-century projections. Hence, this theoretical understanding can facilitate the development of improved 21st-century projections of marine biogeochemistry and ecosystems.

ocean circulation | biogeochemistry | global warming

The Subarctic Atlantic Ocean hosts a highly productive marine ecosystem (1, 2) which contributes to a major regional sink of anthropogenic CO_2 (3) and sustains valuable fisheries along its margins (4). However, Earth system models (ESMs) project that biological productivity will decline rapidly in the Subarctic Atlantic Ocean relative to other oceans as greenhouse gases increase (5, 6). Consistent with these projections, observations suggest that Subarctic Atlantic Ocean productivity has declined during the industrial era (7), but future declines may be far more dramatic (5, 6).

Studies have attributed these rapid regional declines in Subarctic Atlantic Ocean productivity to particularly substantial reductions in the depth of surface mixing layers and a slower Atlantic meridional overturning circulation (AMOC), which led to a vertical decoupling of the surface productivity from the essential nutrients at depth (5, 6, 8). Based on evidence that nutrient transport in the AMOC is important for North Atlantic Ocean productivity (6, 9, 10), some studies recently suggested that the slowing meridional nutrient transport in the North Atlantic Ocean nutrient stream (11–15) (which occurs in conjunction with a slower AMOC) is a stronger physical driver of North Atlantic Ocean productivity declines in 21st-century projections than shoaling surface mixing layers (16, 17). However, the mechanisms that lead to productivity decline in ESMs can be hard to disentangle (5, 6, 16–20), and the relative importance of the physical drivers for the projected 21st-century productivity declines in the Subarctic Atlantic Ocean is not well understood.

Here, we use a two-box theoretical model of the physical and biogeochemical dynamics in the Subarctic Atlantic Ocean to predict and understand the physical drivers of biogeochemical change under increasing ocean surface buoyancy, which results from ocean surface warming and freshening as atmospheric greenhouse gas concentrations increase (5, 19). We also use the box model to interpret sophisticated ESM simulations of marine physical and biogeochemical dynamics in the Subarctic Atlantic Ocean, including the present-day dynamics and 21st-century warming scenarios.

We start by considering the upper layer of our model, which represents the surface mixed layer of the Subarctic Atlantic Ocean, with parameters optimized to reflect present-day conditions (*Materials and Methods*). The annual cycle is the dominant timescale of biogeochemical variability here (21, 22) and therefore an important target for constraining biogeochemical models and improving process understanding. For example, consider the horizontally averaged dynamics of surface nitrate NO_3^-. Although a significant fraction of net primary productivity reflects recycling, nitrate consumption primarily reflects new productivity associated with physical resupply of nutrients that are lost via export of organic material from the surface layer (23). Every winter, after the sun retreats toward the Southern Hemisphere, the Subarctic Atlantic Ocean cools and turbulence mixes water vertically over depths of hundreds of meters (Fig. 1*A*). As a result, the nitrate concentration is relatively high at the surface and fairly well mixed vertically over the top several hundred meters (Fig. 1 *A* and *D*). As the sunlight increases, the surface mixed-layer depth D_s shoals, and the marine ecosystem consumes the nitrate in the surface mixed layer (Figs. 1 *C* and *D* and 2*B*) at a rate

$$\frac{\partial N_s}{\partial t} \approx -\frac{\mathrm{PROD}}{D_s}, \qquad [1]$$

where N_s is the nitrate concentration in the surface mixed layer and PROD is the rate of consumption of nitrate by the ecosystem, i.e., new productivity. As the nitrate is drawn down to relatively low concentrations during summer, new productivity

Significance

Global warming drives cascading changes across physical, chemical, and biological marine systems. However, the coupled dynamics of these systems are difficult to disentangle. Here, we present a simple theoretical model of how these systems respond to global warming in the Subarctic Atlantic Ocean, which experiences particularly dramatic changes in 21st-century warming scenarios. The results reveal how global warming impacts this system by showing that remote changes in the Atlantic basin-scale circulation are a more important driver of biogeochemical change in the Subarctic than local reductions in vertical mixing.

Author contributions: D.B.W. and M.F.J. designed research, performed research, contributed new reagents/analytic tools, analyzed data, and wrote the paper.

The authors declare no competing interest.

This article is a PNAS Direct Submission.

Data deposition: All data and model software are cited in the references and described in *SI Appendix* and Zenodo: http://doi.org/10.5281/zenodo.3757340.

[1]To whom correspondence may be addressed. Email: dwhitt@ucar.edu.

This article contains supporting information online at https://www.pnas.org/lookup/suppl/doi:10.1073/pnas.2000851117/-/DCSupplemental.

First published June 22, 2020.

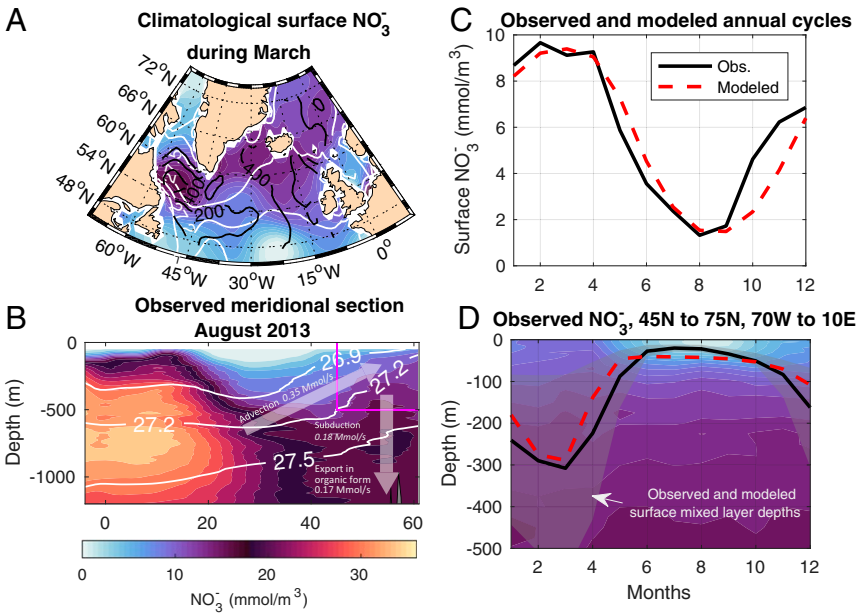

Fig. 1. The box model is optimized to represent observed nitrate NO_3^- concentrations and vertical mixing over the entire Subarctic Atlantic Ocean, from 70°W to 10°E and from 45°N to 75°N. (*A*) A map of the late-winter-maximum surface NO_3^- concentrations from the 2013 World Ocean Atlas (24) and the corresponding March mixed-layer depth (black contours) based on all in situ Argo profiles from 2000 to 2017 (25). (*B*) A hydrographic section of NO_3^- obtained in August 2013 (26). (*C* and *D*) The seasonal cycle of NO_3^- in the World Ocean Atlas (24), which is represented by colored shading in *D*. The mean (black) and 10 to 90% range (gray shading) of the observed mixed-layer depths are plotted in *D*. Modeled values (red dashes) of surface NO_3^- (*C*) and mixed-layer depth (*D*) are plotted for comparison. A few isopycnals are marked by white contours in *A* and *B*. The dominant terms in the present-day nitrogen budget in the Subarctic seasonal thermocline are indicated in *B* (12, 14).

slows (Figs. 1 *C* and *D* and 2*B*). But, as the sunlight reduces again, and the mixed-layer depth D_s deepens during the fall, waters of the seasonal thermocline, which have relatively high nitrate concentrations N_d, are entrained into the surface layer. Thus, the surface nitrate concentration increases (Fig. 1 *C* and *D*) at a rate

$$\frac{\partial N_s}{\partial t} \approx \left(\frac{w_{en}}{D_s}\right)(N_d - N_s), \qquad [2]$$

where the entrainment velocity $w_{en} \approx \partial D_s/\partial t$.

To understand changes in productivity on longer timescales, we also need to consider the model's lower layer, which represents the seasonal thermocline that lies between the summer and the winter mixed-layer depth. This layer holds the essential reservoir of nitrate that is tapped each winter to resupply the surface layer and sustain relatively high rates of new productivity compared to that in subtropical oceans (2, 22) (Fig. 1 *C* and *D*). As a result of the relatively large nitrate reservoir, the seasonal cycle of the nitrate concentration N_d in the seasonal thermocline is far smaller in amplitude than N_s at the surface (Fig. 1*D*). Yet, over an annual cycle, there is a net loss of nitrate via entrainment into the surface layer during fall that is not balanced by the subduction of nitrate from the surface layer into the seasonal thermocline during spring. A near-equilibrium state is sustained by a physical transport of nitrate and remineralization of the production that is exported from the surface layer above into nitrate in the seasonal thermocline.

On interannual and longer timescales, new productivity is constrained by the integrated nitrate budget from the surface to the bottom of the seasonal thermocline (12). A fraction of the new

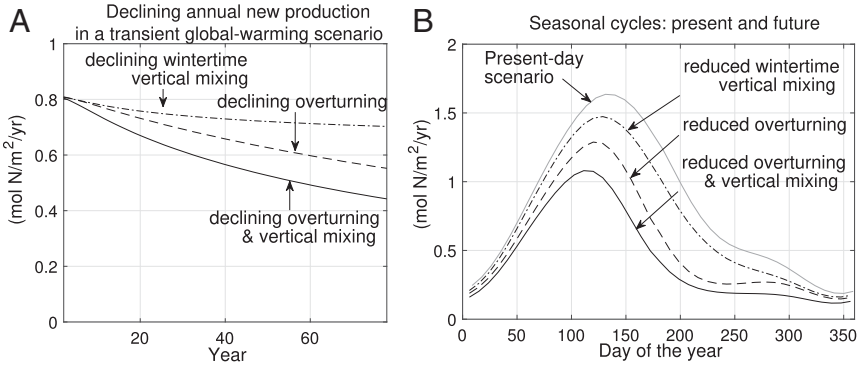

Fig. 2. Future climate scenarios forced by slower overturning and/or shallower winter mixing demonstrate that overturning is the primary driver of lower new productivity. (*A* and *B*) The annual new production in each year (*A*) and the seasonal cycles of new productivity at the beginning and end of the scenarios (*B*). In all three scenarios, surface buoyancy increases at a rate of 4.3×10^{-5} m·s^{-2}·y^{-1}, which is equivalent to a warming of about 0.05 °C/y or a freshening of about 0.005 practical salinity units per year. Note the different *y*-axis ranges.

production is exported below the maximum winter mixed-layer depth, D_w, and thereby lost from the seasonal thermocline. In an equilibrium state, this export to depths below D_w has to be replenished by physical transport processes. Integrated over the upper Subarctic Atlantic Ocean, the physical resupply of nitrate is dominated by advection via the AMOC, which leads us to an approximate mean budget equation for the upper Subarctic Atlantic Ocean:

$$\mathrm{PROD} e^{-D_w/\delta} \approx \frac{\Psi_{max}}{A} \Delta N. \quad [3]$$

Here, δ is the e-folding depth scale over which production is remineralized and $e^{-D_w/\delta}$ is approximately the fraction of new production that is exported below D_w and lost from the seasonal thermocline, which we henceforth call the x ratio; $\Delta N = N_{sub} - N_d$ is the nitrate deficit between the subpolar seasonal thermocline N_d and subtropical thermocline N_{sub} (Fig. 1*B*), Ψ_{max} is the maximum value of the AMOC streamfunction at the subtropical/subpolar boundary (45°N), and $A \approx 11 \times 10^6$ km^2 is the area of the Subarctic Atlantic Ocean (from 45° to 75°N).

By fitting the time-dependent two-box model to the present-day seasonal cycle via optimization, we obtain a model solution that captures the nitrate dynamics of both the surface and seasonal thermocline, as described above (Figs. 1 and 2). *SI Appendix*, Figs. S1–S3 show several additional diagnostics of the optimal solution, including the contributions of each process to the seasonal cycle, i.e., Eqs. **1** and **2**, and the approximately cyclo-stationary equilibrium, i.e., Eq. **3**.

ESMs project that new productivity in the Subarctic Atlantic Ocean will decline over the 21st century in global warming scenarios. The two physical drivers that explain this decline are captured by the box model and highlighted by Eq. **3**: 1) A shoaling of the winter mixed-layer depth D_w leads to an increase in the x ratio such that a larger fraction of the new production is lost from the seasonal thermocline. 2) A slowing of the AMOC volume transport Ψ_{max} leads to a reduction in the resupply of nitrate from the subtropics. For example, in an ensemble of simulations of the Community Earth System Model (CESM) (27) the mean winter mixed-layer depth D_w and the meridional volume transport Ψ_{max} are reduced by about 45 and 54%, respectively, from 2020 to 2100 in a high-emissions scenario (Fig. 3), and qualitatively similar reductions are found in several other ESMs (17). Similar changes in D_w and Ψ_{max} are also predicted by the box model (Fig. 3), which uses a simple first-principles analytic expression (28, 29) to characterize how increasing surface buoyancy drives physically coupled declines in D_w and Ψ_{max} in 21st-century global warming scenarios (*Materials and Methods*).

To separate and quantify the effects of declining D_w and Ψ_{max} on new productivity, we ran the optimized box model through an increasing-buoyancy scenario, which is a simple analog of the high-emissions scenario simulated in the CESM, with different combinations of physical responses: declining D_w with fixed Ψ_{max}, declining Ψ_{max} with fixed D_w, and declining Ψ_{max} and D_w (Fig. 2). The results show that declining D_w and Ψ_{max} both contribute to reduced productivity, with the slowing meridional transport being the increasingly dominant driver of the declining productivity as the surface buoyancy increases. By the end of the 80-y-long integration, the new production is reduced by 0.11 mol N·m^{-2}·y^{-1} if only the mixed-layer shoaling is applied versus 0.26 mol N·m^{-2}·y^{-1} if only the AMOC slowing is applied. If both drivers are applied, the new production is reduced by 0.37 mol N·m^{-2}·y^{-1}. Even though the model dynamics are inherently nonlinear, we therefore empirically find that the effects of AMOC slowing and mixed-layer shoaling approximately add up linearly. In addition, both physical drivers induce qualitatively similar changes in the seasonal cycle of productivity by reducing the peak and shortening the duration of high springtime productivity. The slowing AMOC has a relatively stronger effect than the shoaling mixed layer on both the peak and duration, and the effects of the two drivers on seasonal productivity are approximately additive. Hence, the effects of slowing AMOC and shoaling mixed layers on productivity can be separated with little ambiguity in the box model.

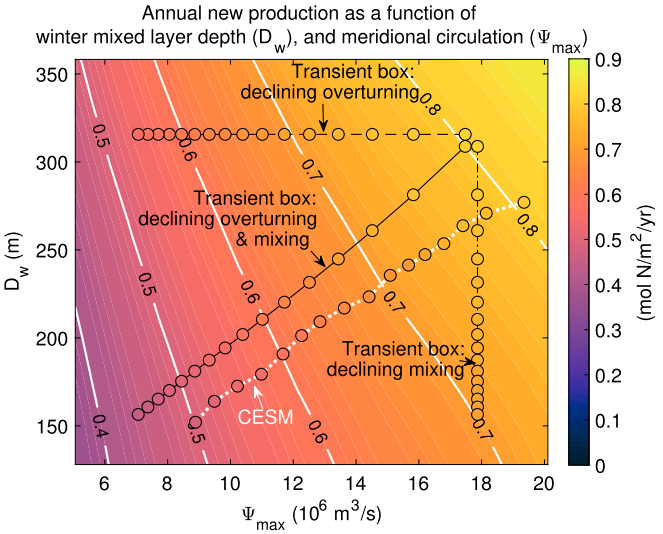

Fig. 3. Model results show the relationship between a shallower winter mixed layer D_w, a slower ocean meridional circulation Ψ_{max}, and reduced new productivity PROD in a warming climate. The background gradient represents the annual new production in equilibrium box model solutions, the three thin black lines are the transient box model solutions in Fig. 2, and the white dotted line is the average over the Subarctic Atlantic Ocean of an ensemble of CESM simulations of the high-emissions representative concentration pathway (RCP8.5) scenario from 2020 to 2100. Circles are marked every 5 y in the transient simulations, with the fill colors again denoting the annual new production. Note that the fill colors are barely distinguishable from the background shading, indicating that 1) the transient simulations are well approximated by the model's equilibrium solution and 2) the ESM results are well approximated by the predictions of the two-box model.

To quantify the potential impact of a wide range of different changes in Ψ_{max} and D_w on new productivity, Fig. 3 shows equilibrium results from the box model as a function of both Ψ_{max} and D_w. Most notably, we find that both the transient box model and the CESM ensemble mean closely follow the equilibrium box-model prediction over the parameter space considered. This is because Eq. **3** holds quite well throughout the transient scenarios (*SI Appendix*, Fig. S4*D*).

To test the robustness of our results, we have quantified the sensitivity of the equilibrium new productivity response to global warming to the most poorly constrained box model parameters. Within observational constraints, the net decline in the annual new production at higher surface buoyancy is relatively robust to the box model parameters (*SI Appendix*, Fig. S5). The x ratio $e^{-D_w/\delta}$ and nitrate deficit ΔN are the most important features of the present-day solutions that control how the physical drivers impact productivity under increasing buoyancy. In particular, if the present-day x ratio and nitrate deficit are reduced, then the shallowing winter mixed layer D_w and hence increasing x ratio have a somewhat greater impact while the slowing meridional circulation Ψ_{max} and hence declining advective nitrate transport $\Psi_{max} N_{sub}$ have a smaller impact, but the net decline in productivity is fairly similar. Nevertheless, declining meridional nitrate transport is the dominant driver of equilibrium productivity declines at the end of the 80-y increasing-buoyancy scenario

shown in Figs. 2 and 3 for all parameter combinations that we considered.

The compensation between sensitivity in the x ratio and nutrient advection may partially explain why ESMs robustly project that new productivity in the Subarctic Atlantic Ocean declines as buoyancy increases, despite substantial differences in the underlying physical and biogeochemical model dynamics (5, 17–19). For example, as shown in *SI Appendix*, Figs. S1 and S4, the CESM has a higher nitrate concentration in the seasonal thermocline and a smaller nitrate deficit than is consistent with observations. In addition, the x ratio in the CESM, as inferred from $e^{-D_w/\delta} \approx 0.33$, is lower than for our box model tuned to observations, where $e^{-D_w/\delta} \approx 0.53$, because the remineralization depth scale is about half as long in the CESM ($\delta \approx 250$ m) compared to the box model ($\delta = 500$ m). In fact, the box model suggests that the higher present-day nitrate concentration in the seasonal thermocline in the CESM is associated with the smaller present-day nitrate deficit, which approximately compensates for the lower x ratio in Eq. **3**. As a result, the annual new production is similar in the box model and the CESM and both have a similar sensitivity to changes in the meridional transport Ψ_{max}. However, other ESMs may differ somewhat from observations and the CESM with regard to the nutrient deficit, the x ratio, and other variables that influence Subarctic Atlantic Ocean productivity declines in 21st-century scenarios (for nutrients, mixed layers, and overturning, see ref. 17). Future analysis of other ESMs could quantify the relevant variables identified by the two-box model to better understand how the drivers of Subarctic Atlantic Ocean productivity decline differ across models.

The physics and biogeochemistry of the Subarctic Atlantic Ocean are projected to undergo rapid change in the coming decades if atmospheric greenhouse gas concentrations continue to increase at current or faster rates. Here, we present a simple predictive theory of the physical and biogeochemical response of the Subarctic Atlantic Ocean to increasing surface buoyancy. The emerging hypotheses are as follows: 1) The simple box model and Eq. **3** capture the most essential dynamics of the productivity response to global warming; numerous other physical, chemical, and ecological changes (5, 18, 19), many of which occur in the CESM, are secondary effects. And, 2) the slower nutrient stream suppresses Subarctic Atlantic Ocean productivity in global warming; the shoaling winter mixed layer and the vertical decoupling of surface productivity from the local deep nutrient reservoir are an important but secondary effect. These results not only provide fundamental insight into the dynamics of the coupled physical/biogeochemical marine systems, but also provide insights into the underlying dynamics of an ensemble of ESM simulations. Such fundamental theoretical understanding of the expected and simulated physical and biogeochemical changes can underpin the development of more accurate and precise projections of the next 10 to 100 y.

Materials and Methods

Two-Box Model. The model (30) simulates the average nitrate concentration NO_3^- in two layers, both of which are above the late-winter maximum surface mixed-layer depth D_w, in the Subarctic Atlantic Ocean. The region has meridional extent $L \approx 2{,}750$ km, zonal extent $W \approx 4{,}000$ km, and area $A = LW \approx 11$ million km^2 (roughly 70°W to 10°E and 45° to 75°N). The coupled governing equations for the evolution of the nitrate concentrations as a function of time in each layer are as follows:

$$\frac{\partial N_s}{\partial t} = \underbrace{-\frac{a\mathrm{PROD}}{D_s}}_{\text{EXPORT PRODUCTION}} \underbrace{-\left(\frac{w_{en}}{D_s}\mathcal{H}(w_{en})\right)(N_s - N_d)}_{\text{ENTRAINMENT}} \underbrace{-\left(\frac{v}{L} + \frac{\kappa_h}{L^2}\right)(N_s - N_{sub})}_{\text{MERIDIONAL TRANSPORT}} \underbrace{-\frac{\kappa_z}{D_s^2}(N_s - N_d)}_{\text{VERT MIX SEAS PYC}}, \quad [4]$$

$$\frac{\partial N_d}{\partial t} = \underbrace{\frac{b\mathrm{PROD}}{D_d}}_{\text{REMINERALIZATION}} \underbrace{-\left(\frac{w_{en}}{D_d}\mathcal{H}(-w_{en})\right)(N_s - N_d)}_{\text{SUBDUCTION}} \underbrace{-\left(\frac{v}{L} + \frac{\kappa_h}{L^2}\right)(N_d - N_{sub})}_{\text{MERIDIONAL TRANSPORT}} \underbrace{+\frac{\kappa_z}{(D_s D_d)}(N_s - N_d)}_{\text{VERT MIX, SEAS PYC}} \underbrace{-\frac{\kappa_z}{(D_s + D_d)D_d}(N_d - N_{aby})}_{\text{VERT MIX, MAIN PYC}}. \quad [5]$$

Export Production and Remineralization. The nitrate concentration N_s in the surface layer with time-varying thickness D_s is drawn down by the ecosystem, which is implicit (as in ref. 31). That is,

$$\mathrm{PROD} = \frac{\mu_m}{k_z} \ln\left(\frac{k_I + I_0}{k_I}\right)\frac{N_s}{k_N + N_s}, \quad [6]$$

where μ_m represents the maximum nitrate consumption rate and k_N is the half-saturation concentration for nitrate uptake. The light limitation function is integrated over D_s, following ref. 21; k_I is the half-saturation irradiance, $1/k_z$ is the e-folding depth, and the annual cycle of photosynthetically available radiation at the sea surface I_0 is defined using standard functions (32) and closely follows satellite observations (30, 33).

Only a fraction $a(D_s)$ of the new production PROD is lost from the surface layer, since a fraction of the new production remineralizes back to N_s within the surface layer. The remineralization of exported production back to nitrate at depth is usually represented via power laws or exponential functions (34). For simplicity, a single exponential function is used to represent the vertical structure of export, such that

$$a = \frac{1}{D_s}\int_{-D_s}^{0} e^{z/\delta}dz = \frac{\delta}{D_s}\left(1 - e^{-D_s/\delta}\right), \quad [7]$$

where δ is the e-folding depth scale over which production is remineralized.

A fraction of the production that is exported from the surface layer is remineralized in the seasonal thermocline, which has nitrate concentration N_d and varying thickness $D_d \approx D_w - D_s$. The fraction of new production that remineralizes in the seasonal thermocline is given by

$$b = a\left(1 - e^{-D_d/\delta}\right). \quad [8]$$

The fraction of new production that is exported to depths below D_w and thereby lost from the seasonal thermocline is given by $a - b \approx e^{-D_w/\delta}$ (*SI Appendix*, Fig. S6), which we call the x ratio, and may range from about 10 to 60% in the Subarctic Atlantic Ocean (35).

Entrainment, Subduction, and Mixed-Layer Depth. The entrainment velocity

$$w_{en} = \frac{\partial D_s}{\partial t} + w(D_s) = \frac{\partial D_s}{\partial t} - v\frac{D_s}{L} \quad [9]$$

is a function of the rate of change of the mixed-layer depth $\partial D_s/\partial t$ and the vertical velocity at the mixed-layer base $w(D_s)$ (36, 37), which is written in terms of the lateral velocity v associated with the incoming AMOC from the south using continuity. As the mixed-layer depth D_s gets shallower during spring, the water formerly in the mixed layer is subducted into the seasonal thermocline. This has no impact on the nitrate concentration in the surface layer (hence the Heaviside function $\mathcal{H}(w_{en})$ in Eq. **4**), but subduction does modify the nitrate concentration in the seasonal thermocline during spring as indicated in Eq. **5**.

Rather than include a prognostic model for the annual cycle of the surface mixed-layer depth D_s, we specify the annual cycle of D_s using an analytic function with parameters controlling the minimum D_b and maximum D_w.

We tune the summertime minimum mixed-layer depth $D_s = D_b$ to provide the best fit to the observed summer (August) nitrate profile (averaged horizontally over the Subarctic Atlantic Ocean) from the World Ocean Atlas 2013 (24). Specifically, we fit the observed nitrate profile over the upper 200 m, using a step function:

$$N(z) = \begin{cases} N_s & z \le D_b \\ N_d & z > D_b. \end{cases} \quad [10]$$

Since the true horizontally averaged mixed-layer concentration is best approximated by the averaged surface value, we prescribe that $N_s = N^{obs}(z=0) = 1.3$ mmol/m^3, but we optimize D_b and N_d to minimize $(N(z) - N^{obs}(z))^2$ averaged over the top 200 m. The best fit is obtained for $N_d = 11.3$ mmol/m^3 and $D_b = 40$ m; the latter is hence used in all our experiments. The maximum late-winter mixed-layer depth D_w is determined via an optimization procedure described below, and the result is an annual cycle in D_s that is very similar to the observed spatially averaged mixed-layer depth as shown in Fig. 1*D* (the observations are based on all Argo profiles from the years 2000 to 2017 and published in ref. 25).

Meridional Nitrate Transport. A northward mean velocity v and horizontal eddy/gyre mixing with diffusivity κ_h restore upper-ocean nitrate in the Subarctic Atlantic Ocean toward the high nitrate concentration N_{sub} on the same isopycnals in the permanent thermocline at lower latitudes (Fig. 1*B*) (11, 12, 15–17). In the present climate, the advective timescale $L/v = AD_w/\Psi_{max} \sim 6$ y, where $\Psi_{max} \approx 18$ sverdrups (Sv) is an estimate of the northward volume transport in the Atlantic meridional overturning circulation based on observational constraints (38). This estimate of the overturning seems fairly well constrained (within ± 2 Sv) for the present day and is therefore not considered a tunable parameter. The horizontal diffusive timescale is less well constrained by observations but is thought to be at least an order of magnitude longer than L/Ψ_{max}. Here, we assume $\kappa_h = 2{,}500$ m^2/s, which gives a diffusive timescale $L^2/\kappa_h \sim 100$ y.

The overturning velocity scale is physically coupled to the mixed-layer depth and the surface buoyancy following ref. 28. In particular, we define the depth scale of the upper limb of the AMOC or, equivalently, the maximum depth of wintertime convection by matching the minimum surface buoyancy in the Subarctic Atlantic Ocean to the buoyancy profile in the basin's lower latitudes (*SI Appendix*, Fig. S7). Assuming an exponential low-latitude buoyancy profile $b_{LL} = b_S \exp(z/h)$ yields an AMOC depth scale

$$D_{MOC} = h \ln b_S/b_N, \qquad [11]$$

where b_N is the surface buoyancy in the northern deep water formation region. Then, $D_w = R_{winter} D_{MOC}$, where R_{winter} is a scaling factor that is determined via optimization to reduce the spatially variable maximum winter mixed-layer depth to a single representative value D_w.

The overturning streamfunction can be estimated using

$$\partial_{zz}\Psi = \frac{1}{f_0}[b_N - b_{LL}] \qquad [12]$$

for $-D_{MOC} < z < 0$, with the boundary conditions $\Psi(0) = \Psi(-D_{MOC}) = 0$. The solution to Eq. **12** with boundary conditions applied is

$$\Psi(z) = \frac{b_S}{f_0}\left[h^2(1 - \exp(z/h)) + \frac{\alpha}{2}(D_{MOC} + z)z + \frac{h^2(1-\alpha)}{D_{MOC}}z\right], \qquad [13]$$

where $\alpha \equiv b_N/b_S$, and D_{MOC} is given by Eq. **11**.

We are here interested in the total overturning transport, that is, the maximum of $\Psi(z)$. Unfortunately, analytically solving for the maximum of Eq. **13** is not straightforward, but, as shown in *SI Appendix*, Fig. S8, the maximum value of the overturning streamfunction is very well approximated as

$$\Psi_{max} \approx \frac{0.052(b_S - b_N)}{f_0(D_{MOC}^{-2} + 0.073\ h^{-2})}. \qquad [14]$$

Using $b_S = 0.0205$ m/s^2, $b_N = 0.0005$ m/s^2, $h = 500$ m, $f_0 = 10^{-4}$ s^{-1}, which we hold fixed in present-day scenarios, the maximum magnitude of the AMOC streamfunction $\Psi_{max} = 17.9$ Sv compares well with observational estimates (38).

Vertical Diffusion. Vertical mixing in the thermocline restores the nitrate in the seasonal thermocline N_d toward the abyssal concentration $N_{aby} \approx 18$ mmol/m^3 and mixes nitrate between the model layers. This mixing is represented via a diffusive process with $\kappa_z = 2 \times 10^{-5}$ m^2/s based on observations (39). The flushing timescales are $D_b^2/\kappa_z \sim 3$ y for transport from the seasonal thermocline to the summertime mixed layer and $D_w^2/\kappa_z \sim 160$ y for transport from the deep ocean to the seasonal thermocline.

Other Sources/Sinks. Additional sources and sinks of nitrate to the seasonal thermocline and surface mixed layer of the Subarctic Atlantic Ocean, which include meridional advection and remineralization of oceanic organic nitrogen, microbial nitrogen fixation and denitrification, nitrogen deposition from the atmosphere or sea ice, and riverine/sedimentary input in shallow water, are thought to be much smaller than the advective nitrate transport to the seasonal thermocline via the AMOC. Therefore, these sources/sinks will not impact the results presented here and are omitted from the box model for simplicity but included (with the exception of coastal riverine/sedimentary inputs) in the CESM, which is described in more detail below.

21st-Century Scenarios. Global warming scenarios are implemented in the box model by increasing the surface buoyancies b_S and b_N, which impact $D_w = R_{winter} D_{MOC}$ via Eq. **11** and Ψ_{max} via Eq. **14**. For simplicity, both b_S and b_N are increased at the same rate, although the results are primarily sensitive to changes in b_N. These simple relations are expected to adequately describe the transient response of D_w and Ψ_{max} to increasing surface buoyancy on timescales from order 10 to 100 y, i.e., over several decades. On shorter timescales, AMOC variability becomes meridionally incoherent and is significantly influenced by processes that are not incorporated in this simple model (38). Similarly, the mixed-layer depth variability will not necessarily be coherent with the circulation on short timescales. Conversely, on longer timescales of centuries to millennia, the deep ocean will adjust to changes in buoyancy, thus invalidating the assumptions made in the physical model (29, 40). In addition, N_{sub} tends to decline with warming (6, 17), which is not considered in our box-model warming scenarios but is accounted for in the CESM. A sensitivity study suggests this effect has a smaller impact on 21st-century productivity than either declining D_w or Ψ_{max} (*SI Appendix*, Fig. S9), but the effect may be more significant on longer timescales, e.g., due to teleconnections to the Southern Ocean (6, 10).

Parameter Optimization. Despite the simplicity of the box model, it has several parameters that are not very well constrained by direct observational estimates. These include the upstream nitrate concentration in the subtropical thermocline, N_{sub} (12 to 22 mmol/m^3); the maximum nitrate consumption rate, μ_m (0.1 to 1.5 mmol/m^3/d); the half-saturation constant for nitrate uptake, k_N (0.5 to 8 mmol/m^3); the ratio of the winter mixed-layer depth to the AMOC depth scale, $R_{winter} = D_w/D_{MOC}$ (0.05 to 0.5); and the e-folding depth scale over which remineralization occurs, δ (50 to 750 m). Hence, we identify the optimal model parameters indirectly by obtaining a five-dimensional hypercube of 12^5 model solutions with a range of 12 values for each parameter given in parentheses above. For each of the 12^5 parameter combinations, a 115-y simulation is run from initial conditions with $N_s = N_d = 10$ mmol/m^3 under present-day boundary conditions. The last annual cycle, when the solution is effectively cyclo-stationary, is used for model evaluation.

We identify reasonable values for the parameters by comparing these solutions with observational constraints and minimizing a cost function that is a sum of squared errors. The set of parameters that minimizes this cost function and is used to produce the results in Figs. 1–3 is given in *SI Appendix*, Table S1.

The first set of constraints is derived from observation-based estimates of nitrate and new production. The surface nitrate concentration in the Subarctic Atlantic Ocean reaches a minimum of 1.3 mmol/m^3 in August and a maximum of 9.7 mmol/m^3 in February (24). And the best fit to the nitrate concentration in the seasonal thermocline is obtained for a value of $N_d = 11.3$ mmol/m^3 (see above). Thus, we define the following three cost functions: $C_1 = [(\min_{month}(N_s) - 1.3)/2]^2$, $C_2 = [(\max_{month}(N_s) - 9.7)/2]^2$, and $C_3 = [(\text{mean}(N_d) - 11.3)/2]^2$. We normalize each difference by dividing by our estimates of the uncertainty, which we define based on our judgment of the uncertainties associated with structural differences between the model formulation and the real system which are at least as large as the various sampling and measurement uncertainties. Observational estimates of new production range fairly widely, but it is unlikely that the true regional and annual average is outside the range 0.1 to 1.4 mol N·m^{-2}·y^{-1} and it is most likely toward the middle of this range (2, 22, 41, 42). Based on these references we define a cost function $C_4 = [(\text{mean}(\text{PROD}) - 0.7)/0.7]^2$.

We find that the parameters are not uniquely defined by the constraints C_1 to C_4. The 1,000 solutions with the smallest summed cost do not cluster around a single point in the five-dimensional parameter space, but rather define a multidimensional subspace of plausible parameter sets (*SI Appendix*, Fig. S6). Specifically, the good solutions fall on a diagonal through μ_m-k_N parameter space covering essentially all values that we consider for

each of μ_m and k_N. In addition, for given values of k_N and μ_m, there are good solutions along a diagonal in D_w/δ-N_{sub} parameter space. In addition, changes in δ can also be compensated by changes in D_w, independent of the other parameters.

As a result, we find that three additional constraints are required, one on k_N or μ_m, one on N_{sub} or δ/D_w, and one on δ or D_w, if we want to determine a unique set of most likely model parameters. Fortunately, laboratory experiments and observations do provide guidance about the most appropriate values of k_N, δ, and N_{sub}. Observations that the Subarctic Atlantic Ocean is dominated by larger phytoplankton (43, 44) suggest an additional term for our cost function as $C_5 = [(k_N - 3)/3]^2$. Second, observations suggest that the incoming nitrate flux $N_{sub}\Psi_{max}$ is between 300 and 400 kmol/s (11, 12, 16), so we impose the constraint $N_{sub} = (300–400)$ kmol s^{-1}/18 Sv = 17 to 22 mmol/m^3, which suggests $C_6 = [(N_{sub} - 19.5)/2.5]^2$. Finally, observations that the attenuation of sinking particulate organic material has a depth scale toward the middle of the 100- to 1,000-m range (34) suggest $C_7 = [(\delta - 500)/300]^2$. With these three additional constraints, C_5 to C_7, we find that the solutions with smallest summed cost cluster narrowly in all parameters. The best solution (out of 12^5) has a summed cost $\sum_{i=1}^{7} C_i = 0.19$ and the parameters are listed in *SI Appendix*, Table S1. This "best" present-day solution is obtained by running a 200-y simulation to equilibrium; diagnostics are in Figs. 1 and 2 and *SI Appendix*.

We also find that the equilibrium annual new production at higher surface buoyancy is not very sensitive to the specific parameter targets C_5 to C_7. To demonstrate this, we simulate the late-time cyclo-stationary response to an instantaneous increase in surface buoyancy for several different parts of k_N-μ_m, N_{sub}-D_w/δ, and δ-D_w parameter space (*SI Appendix*, Fig. S5); the relationships between each parameter pair are constrained by C_1 to C_4 (*SI Appendix*, Fig. S6). The overall response to increasing surface buoyancy is very similar for a fairly wide range of these parameters, and the slowing meridional nitrate transport is generally more important than the shoaling mixed layer and the resulting decoupling of the surface mixed layer from the local deep nitrate reservoir.

CESM. Box-model results are compared with a large ensemble of simulations of the high-emissions RCP8.5 scenario with the CESM, a sophisticated ESM. The members of this ensemble differ only due to the introduction of small random noise in the year 1920, and the model and experimental protocol are described in detail in ref. 27.

All results are averaged over 32 members with valid biogeochemistry and over the area from 70°W to 10°E and 45°N to 75°N. New productivity PROD is approximated by vertically summing the net biogeochemical nitrate tendency over the top 50 m, where this tendency is negative. Below 50 m, the nitrate tendency is positive due to remineralization, and the vertical profile of this tendency has an e-folding depth scale similar to the particulate organic nitrogen flux $\delta_{CESM} \approx 250$ m (*SI Appendix*, Fig. S4C). The AMOC streamfunction Ψ and nitrate flux function are calculated by averaging the monthly output in potential density space, as described in ref. 16 and shown in figure 6 in ref. 16. The winter mixed-layer depth D_w is calculated using the same definition as for the observations (25).

Data Availability. All data and model software are cited in the references and described in *SI Appendix* and Zenodo: http://doi.org/10.5281/zenodo.3757340.

ACKNOWLEDGMENTS. This material is based upon work supported by the National Center for Atmospheric Research (NCAR), which is a major facility sponsored by the National Science Foundation (NSF) under Cooperative Agreement 1852977. Travel funding from NCAR, via the Climate and Global Dynamics Laboratory, made this collaboration possible. D.B.W. was supported by the NSF, via Contract OCE-1658541, as well as by the National Oceanic and Atmospheric Administration via Contract NA18OAR4310408. M.F.J. acknowledges support from the NSF via Award OCE-1846821.

1. C. B. Field, M. J. Behrenfeld, J. T. Randerson, P. Falkowski, Primary production of the biosphere: Integrating terrestrial and oceanic components. *Science* **281**, 237–240 (1998).
2. T. DeVries, T. Weber, The export and fate of organic matter in the ocean: New constraints from combining satellite and oceanographic tracer observations. *Global Biogeochem. Cycles* **31**, 535–555 (2017).
3. C. L. Sabine *et al.*, The oceanic sink for anthropogenic CO2. *Science* **305**, 367–371 (2004).
4. D. A. Kroodsma *et al.*, Tracking the global footprint of fisheries. *Science* **359**, 904–908 (2018).
5. L. Bopp *et al.*, Multiple stressors of ocean ecosystems in the 21st century: Projections with CMIP5 models. *Biogeosciences* **10**, 6225–6245 (2013).
6. J. K. Moore *et al.*, Sustained climate warming drives declining marine biological productivity. *Science* **359**, 1139–1143 (2018).
7. M. B. Osman *et al.*, Industrial-era decline in subarctic Atlantic productivity. *Nature* **569**, 551–555 (2019).
8. A. Schmittner, Decline of the marine ecosystem caused by a reduction in the Atlantic overturning circulation. *Nature* **434**, 628–633 (2005).
9. J. Sarmiento, N. Gruber, M. Brzezinski, J. Dunne, High-latitude controls of thermocline nutrients and low latitude biological productivity. *Nature* **427**, 56–60 (2004).
10. B. Bronselaer, L. Zanna, D. R. Munday, J. Lowe, The influence of Southern Ocean winds on the North Atlantic carbon sink. *Global Biogeochem. Cycles* **30**, 844–858 (2016).
11. J. L. Pelegrí, G. T. Csanady, Nutrient transport and diapycnal mixing in the Gulf Stream. *J. Geophys. Res.* **96**, 2577–2583 (1991).
12. R. G. Williams, V. Roussenov, M. J. Follows, Nutrient streams and their induction into the mixed layer. *Global Biogeochem. Cycles* **20**, GB1016 (2006).
13. J. Palter, S. Lozier, On the source of Gulf Stream nutrients. *J. Geophys. Res.* **113**, C06018 (2008).
14. R. G. Williams *et al.*, Nutrient streams in the North Atlantic: Advective pathways of inorganic and dissolved organic nutrients. *Global Biogeochem. Cycles* **25**, GB4008 (2011).
15. J. L. Pelegrí, I. Vallès-Casanova, D. Orúe-Echevarría, "The gulf nutrient stream" in *Kuroshio Current: Physical, Biogeochemical, and Ecosystem Dynamics*, Geophysical Monograph 243, T. Nagai, H. Saito, K. Suzuki, M. Takahashi, Eds. (John Wiley & Sons, Inc. Hoboken, NJ, 2019), pp. 23–50.
16. D. B. Whitt, "On the role of the gulf stream in the changing Atlantic nutrient circulation during the 21st century" in *Kuroshio Current: Physical, Biogeochemical, and Ecosystem Dynamics*, Geophysical Monograph 243, T. Nagai, H. Saito, K. Suzuki, M. Takahashi, Eds. (John Wiley & Sons, Inc. Hoboken, NJ, 2019), pp. 51–82.
17. F. Tagklis, T. Ito, A. Bracco, Modulation of the North Atlantic deoxygenation by the slowdown of the nutrient stream. *Biogeosciences* **17**, 231–244 (2020).
18. C. Laufkötter *et al.*, Projected decreases in future marine export production: The role of the carbon flux through the upper ocean ecosystem. *Biogeosciences* **13**, 4023–4047 (2016).
19. W. Fu, J. T. Randerson, J. K. Moore, Climate change impacts on net primary production (NPP) and export production (EP) regulated by increasing stratification and phytoplankton community structure in the CMIP5 models. *Biogeosciences* **13**, 5151–5170 (2016).
20. W. Fu, F. Primeau, J. Keith Moore, K. Lindsay, J. T. Randerson, Reversal of increasing tropical ocean hypoxia trends with sustained climate warming. *Global Biogeochem. Cycles* **32**, 551–564 (2018).
21. G. T. Evans, J. S. Parslow, A model of annual plankton cycles. *Biol. Oceanogr.* **3**, 327–347 (1985).
22. R. G. Williams, A. J. McLaren, M. J. Follows, Estimating the convective supply of nitrate and implied variability in export production over the North Atlantic. *Global Biogeochem. Cycles* **14**, 1299–1313 (2000).
23. R. W. Eppley, B. J. Peterson, Particulate organic matter flux and planktonic new production in the deep ocean. *Nature* **282**, 677–680 (1979).
24. H. E. Garcia *et al.*, *World Ocean Atlas 2013, Volume 4: Dissolved Inorganic Nutrients (phosphate, nitrate, silicate)*, NOAA Atlas NESDIS, S. Levitus, A. Mishonov Eds. (US Department of Commerce, Silver Spring, MD, Tech. Rep. 76).
25. D. Whitt, S. Nicholson, M. Carranza, Global impacts of subseasonal (< 60 day) wind variability on ocean surface stress, buoyancy flux, and mixed layer depth. *J. Geophys. Res. Oceans* **124**, 8798–8831 (2019).
26. J. Zang, C. Mordy, Bottle data from cruise A16N, WHP netcdf version. https://cchdo.ucsd.edu/cruise/33ro20130803. Accessed 25 August 2019.
27. J. E. Kay *et al.*, The Community Earth System Model (CESM) large ensemble project: A community resource for studying climate change in the presence of internal climate variability. *Bull. Am. Meteorol. Soc.* **96**, 1333–1349 (2015).
28. M. Nikurashin, G. Vallis, A theory of the interhemispheric meridional overturning circulation and associated stratification. *J. Phys. Oceanogr.* **42**, 1652– 1667 (2017).
29. M. F. Jansen, L. P. Nadeau, A toy model for the response of the residual overturning circulation to surface warming. *J. Phys. Oceanogr.* **49**, 1249–1268 (2019).
30. D. B. Whitt, M. F. Jansen, Software for "slower nutrient stream suppresses Subarctic Atlantic biological productivity in global warming." Zenodo. http://doi.org/10.5281/zenodo.3757340. Deposited 15 January 2020.
31. G. A. McKinley, M. J. Follows, J. Marshall, Mechanisms of air-sea CO2 flux variability in the equatorial Pacific and the North Atlantic. *Global Biogeochem. Cycles* **18**, GB2011 (2004).
32. R. M. Green, *Spherical Astronomy* (Cambridge University Press, 1985).
33. OBPG NASA Goddard Space Flight Center, Ocean Ecology Laboratory, Moderate-resolution imaging spectroradiometer (MODIS) Aqua par data (2018) (NASA OB.DAAC, Greenbelt, MD). https://doi.org/10.5067/AQUA/MODIS/L3B/PAR/2018. Accessed 29 August 2019.
34. R. A. Armstrong, C. Lee, J. I. Hedges, S. Honjo, S. G. Wakeham, A new, mechanistic model for organic carbon fluxes in the ocean based on the quantitative association of POC with ballast minerals. *Deep Sea Res. II* **49**, 219–236 (2001).
35. H. I. Palevsky, D. P. Nicholson, The North Atlantic biological pump: Insights from the ocean observatories initiative Irminger Sea Array. *Oceanography* **31**, 42–49 (2018).
36. B. Cushman-Roisin, "Subduction" in *Dynamics of the Ocean Mixed Layer*, P. Müller, D. Henderson, Eds. (Special Publication, Hawaii Institute for Geophysics, 1987), pp. 181–196.

37. J. C. Marshall, R. G. Williams, A. G. Nurser, Inferring the subduction rate and period over the North Atlantic. *J. Phys. Oceanogr.* **23**, 1315–1329 (1993).
38. P. Cessi, The global overturning circulation. *Annu. Rev. Mar. Sci.* **11**, 249–270 (2019).
39. A. P. Martin *et al.*, The supply of nutrients due to vertical turbulent mixing: A study at the porcupine abyssal plain study site in the northeast Atlantic. *Deep Sea Res. Part II Top. Stud. Oceanogr.* **57**, 1293–1302 (2010).
40. M. F. Jansen, L. P. Nadeau, T. M. Merlis, Transient versus equilibrium response of the ocean's overturning circulation to warming. *J. Clim.* **31**, 5147–5163 (2018).
41. W. Koeve, Wintertime nutrients in the North Atlantic—new approaches and implications for new production estimates. *Mar. Chem.* **74**, 245–260 (2001).
42. P. Quay, J. Stutsman, T. Steinhoff, Primary production and carbon export rates across the subpolar N. Atlantic Ocean basin based on triple oxygen isotope and dissolved O2 and Ar gas measurements. *Global Biogeochem. Cycles* **26**, GB2003 (2012).
43. K. F. Edwards, M. K. Thomas, C. A. Klausmeier, E. Litchman, Allometric scaling and taxonomic variation in nutrient utilization traits and maximum growth rate of phytoplankton. *Limnol. Oceanogr.* **57**, 554–566 (2012).
44. A. D. Barton *et al.*, The biogeography of marine plankton traits. *Ecol. Lett.* **16**, 522–534 (2013).